ChemComm

COMMUNICATION

View Article Online
View Journal | View Issue

Open Access Article. Published on 16 July 2025. Downloaded on 5/23/2026 10:59:14 AM.
This article is licensed under a Creative Commons Attribution-NonCommercial 3.0 Unported Licence.

Check for updates

Cite this: *Chem. Commun.*, 2025, **61**, 12566

Received 17th March 2025,
Accepted 16th July 2025

DOI: 10.1039/d5cc01366f

rsc.li/chemcomm

Stabilisation and functional enhancement of a metal–organic framework purinate-glass composite†

Yujun Rong,‡[a] Ashleigh M. Chester, ‡[a] Bethan Turner, [b] Georgina P. Robertson,[ac] Ayano Kono,[a] Philip A. Chater, [c] Lauren N. McHugh, [b] David A. Keen, [d] Thomas D. Bennett[ae] and Celia Castillo-Blas §*[a]

The development of metal–organic framework (MOF) crystal-glass composites (CGCs) has been hindered by the scarcity of MOF glass matrices with low glass transition temperatures (T_gs). Here, we investigate a CGC consisting of a low-T_g MOF glass (a_gZIF-UC-7) and UiO-66. Powder X-ray diffraction and stability tests in phosphate buffer saline solution showed UiO-66 was stabilised in the glass matrix. Additionally, the composite exhibited enhanced dye uptake and gas adsorption relative to a_gZIF-UC-7.

Metal–organic frameworks (MOFs) are nanoporous materials formed by the self-assembly of metal ion-based nodes and organic linkers.[1] They have exhibited promise in a variety of applications, including gas separation, catalysis and biomedicine.[2] The biomedical application of MOFs has gained interest because of their tuneable pore size and chemistry, achieved by combining different nodes and linkers. For example, MOFs can be used to store and release drugs, influence inflammatory wound environments and can be used in implants for improving host-tissue implant interfaces.[3] To develop biocompatible MOFs, it is essential to use building blocks such as bioactive metal ions (*e.g.* Zr^{4+}, Zn^{2+} or Fe^{2+}) and bioactive organic linkers such as amino acid, peptides, nucleobases and saccharides.

Zeolitic imidazolate frameworks (ZIFs) are a subclass of MOFs consisting of tetrahedrally-coordinated metal ions (Zn^{2+}, Co^{2+}, Mn^{2+}, Fe^{2+}) linked by imidazolate (Im^-) derivatives. Several ZIFs can form glasses, such as ZIF-62[4] $[Zn(Im)_{1-x}(bIm)_x]$ (Im = imidazolate, bIm = benzimidazolate, $0.1 < x < 0.33$).[5,6] These hybrid glasses can be defined as amorphous solids that exhibit a heat-induced transition from a brittle to a viscoelastic state over a temperature range given by the glass transition temperature (T_g).

Recently, ZIFs consisting of bioactive cations such as Zn^{2+} and biocompatible linkers such as purine, a family of nucleobases, have been successfully developed. Examples include ZIF-UC-7, $[Zn(Im)_x(pur)_{2-x}]$ (pur = purinate), [Zn(pur, nIm)] (nIm = 4-nitro-2-phenoxymethanesulfonanilide) and [Zn(pur)Br·0.25DMF].[7–9] Purine-containing ZIFs have both potential bioactivity and glass-forming ability, which might be promising for the fabrication of bioactive hybrid glasses. ZIF-UC-7 displays excellent glass forming ability thanks to its relatively low T_g and T_m compared to other meltable ZIFs. Despite their functional advantages in biomedical applications,[10] MOFs are limited by their chemical instability and poor processability to form bulk products and are typically synthesised as microcrystalline powders.[11]

To address these manufacture limitations, MOF composites have received increased attention in the last years.[12,13] One of the methods for manufacturing bulk MOF-derived materials is dispersing MOF crystals in a polymer matrix to fabricate mixed matrix membranes (MMMs).[14] However, MMMs have various limitations, such as the formation of interfacial mesoporous voids and aggregation of MOF components within the matrix.[15]

Due to their excellent compatibility with crystalline MOFs, MOF glasses have been suggested as an alternative to polymer matrices.[16] MOF crystal-glass composites (MOF CGCs), combining both crystalline and glassy MOFs, have shown improved gas adsorption properties relative to the MOF glass,[17] where MOF glasses typically have reduced porosity relative to their parent crystals. Here, we investigate a new MOF CGC comprising a

[a] *Department of Materials Science and Metallurgy, University of Cambridge, Cambridge, CB3 0FS, UK. E-mail: castillo@icmm.csic.es*
[b] *Department of Chemistry, University of Liverpool, Crown Street, Liverpool L69 7ZD, UK*
[c] *Diamond Light Source Ltd, Diamond House, Oxfordshire, OX11 0DE, UK*
[d] *ISIS Facility, Rutherford Appleton Laboratory, Harwell Campus, Didcot, Oxfordshire OX11 0QX, UK*
[e] *School of Physical and Chemical Sciences, University of Canterbury, Private Bag 4800, Christchurch 8140, New Zealand*

† Electronic supplementary information (ESI) available. See DOI: https://doi.org/10.1039/d5cc01366f

‡ Both authors contributed equally.

§ Present address: Materials Science Institute of Madrid – Spanish National Research Council (ICMM-CSIC), C/Sor Juana Inés de la Cruz 3, Madrid, 28049, Spain.

 This journal is © The Royal Society of Chemistry 2025

Open Access Article. Published on 16 July 2025. Downloaded on 5/23/2026 10:59:14 AM.
This article is licensed under a Creative Commons Attribution-NonCommercial 3.0 Unported Licence.

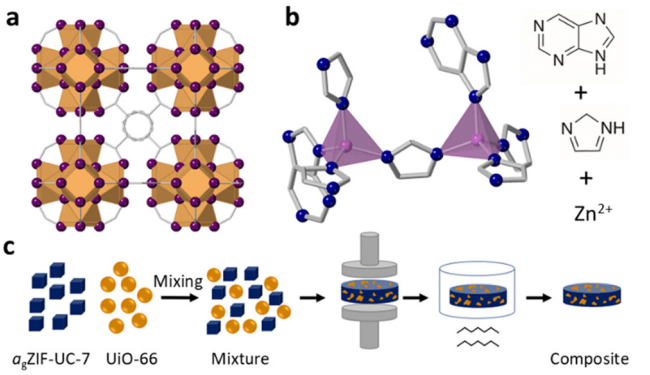

Fig. 1 (a) UiO-66 structure (Zr-orange tetrahedra, C-grey, O-purple), (b) ZIF-UC-7 structure and precursors (Zn-purple, C-grey, N-blue), (c) Scheme of the MOF-CGC fabrication.

bioactive MOF glass matrix (a_gZIF-UC-7), selected for its low T_g (273 °C) and bioactive linker.[7] Selecting a lower T_g glass means a lower working temperature (T_w) can be used because the T_w must exceed the T_g of the glass to facilitate composite formation. The composite was synthesised using a previous methodology (Fig. 1). Specifically, UiO-66, $[Zr_6O_4(OH)_4(BDC)_6{\cdot}xH_2O]$ (UiO = Universitetet i Oslo; BDC = 1,4-benzene dicarboxylic acid), was dispersed into the glass matrix; UiO-66 was selected because of its high surface area (1050 $m^2\ g^{-1}$) and thermal stability (stable up to 500 °C).[18]

ZIF-UC-7 was synthesised solvothermally (Fig. S1, ESI†), with powder X-ray diffraction (PXRD) confirming its crystalline structure (Fig. S2 and Table S1, ESI†).[7] CHN analysis and solution state ^{1}H NMR (acid digested) support the $[Zn(Im)_{1.75}(pur)_{0.25}]$ formula (Table S2 and Fig. S3, ESI†). Thermogravimetric analysis (TGA) of the crystalline ZIF-UC-7 shows a thermal decomposition temperature (T_d) of 521 °C (Fig. S4, ESI†). Differential scanning calorimetry (DSC) confirmed the melting temperature (T_m) and T_g (Fig. S5, ESI†). The first DSC upscan of crystalline ZIF-UC-7 shows a T_m of 336.7 °C and the second DSC scan shows a T_g of 273.1 °C, consistent with the literature.[7] a_gZIF-UC-7, formed by melt-quenching, shows no Bragg peaks in its PXRD (Fig. 2a and Fig. S6, ESI†), confirming its amorphous nature. DSC analysis on a_gZIF-UC-7 shows T_gs of 277 and 278 °C in the first and second upscans respectively (Fig. S5, ESI†); TGA shows a T_d of ∼507 °C (Fig. S7, ESI†). Fourier-transform infrared spectroscopy (FTIR) and ^{1}H NMR (acid-digested) of a_gZIF-UC-7 and ZIF-UC-7 confirm retention of the chemical features post-melt-quenching (Fig. S8 and S9, ESI†). UiO-66 was synthesised based on reported methods; its structure was confirmed by Pawley refinement of the PXRD data (Fig, S10 and Table S3, ESI†). TGA shows a T_d of ∼350 °C (Fig. S11, ESI†), giving a working range for composite formation of $278 < T_w < 350$ °C; a T_w of 300 °C was selected to reduce loss of Bragg peak intensities (Fig. S12, ESI†). The working pressure was 0.074 GPa to minimise Bragg peak broadening (Fig. S13, ESI†). With these working parameters, equal weight percentages (wt%) of the starting materials were ball-milled to form a physical mixture, defined as (UiO-66)(a_gZIF-UC-7)(50/50). This mixture was then pelletised and heated to 300 °C, exceeding the

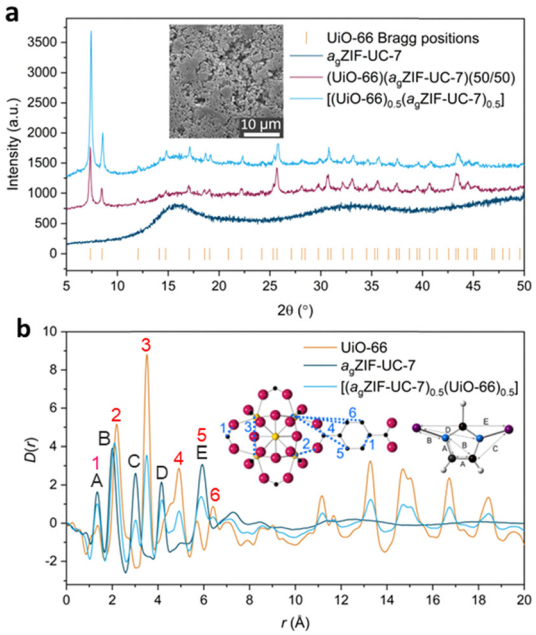

Fig. 2 (a) PXRD of the physical mixture and composite, inset: SEM image of composite and (b) X-ray PDFs, $D(r)$s, of the composite and starting materials, insets show the $Zr_6O_4(OH)_4$ cluster and BDC linker of UiO-66 (Zr-yellow, C-black, O-pink) and imidazolate of a_gZIF-UC-7 (Zn-purple, C-black, N-blue, H-white).

T_g of a_gZIF-UC-7, enabling it to enter its supercooled liquid state and embed the UiO-66 crystallites. After cooling under vacuum, a cohesive, non-powdery $[(UiO\text{-}66)_{0.5}(a_g ZIF\text{-}UC\text{-}7)_{0.5}]$ composite was produced (Fig. S17, ESI†).

PXRD (Fig. 2a) shows UiO-66 Bragg peaks in both the (UiO-66)(a_gZIF-UC-7)(50/50) and $[(UiO\text{-}66)_{0.5}(a_g ZIF\text{-}UC\text{-}7)_{0.5}]$ patterns, confirming UiO-66 crystallinity post composite synthesis. Bragg intensity is maintained after pelletisation and increases after heating (Fig. S14, ESI†). The lattice parameters extracted from Pawley refinement match the literature values, indicating retention of the UiO-66 structure in the composite (Fig. S15 and Table S4, ESI†). In contrast, the UiO-66 controls show no such preservation (Fig. S13, ESI†), suggesting that the a_gZIF-UC-7 matrix stabilised the UiO-66 structure under pressure and heat. FTIR also confirms the presence of a_gZIF-UC-7 and UiO-66 in both the physical mixture and composite (Fig. S16, ESI†). CHN and ICP analysis confirmed the composite and physical mixture compositions. The composite matched the target $[(UiO\text{-}66)_{0.50}\text{-}(a_g ZIF\text{-}UC\text{-}7)_{0.5}]$ composition (Tables S5–S7, ESI†). Similar ICP results for the physical mixture and composite indicate minimal decomposition of the a_gZIF-UC-7 component during composite formation after the thermal treatment.

The starting materials, physical mixture and composite were analysed by optical microscopy (Fig. S18 and S19, ESI†) and SEM (Fig. S20–S30, ESI†). SEM images of the (UiO-66)(a_gZIF-UC-7)(50/50) physical mixture show UiO-66 crystallites on the a_gZIF-UC-7 surface (Fig. S21, ESI†). The pelletised physical mixture shows UiO-66 and a_gZIF-UC-7 particles (Fig. S22, ESI†). Heating to 300 °C (above T_g = 278 °C) forms a composite with flow marks and UiO-66 crystallites embedded in the matrix

Open Access Article. Published on 16 July 2025. Downloaded on 5/23/2026 10:59:14 AM.
This article is licensed under a Creative Commons Attribution-NonCommercial 3.0 Unported Licence.

(Fig. 2 inset; Fig. S23, ESI†). The composite surface is not uniform, likely because of the low pelletisation pressure limiting contact between a_gZIF-UC-7 and UiO-66. EDX (Fig. S24–S26, ESI†) shows similar Zr : Zn ratios (∼1.4–1.6) for both the pelletised physical mixture and composite, again suggesting minimal decomposition. Smaller regions (10–30 μm) reveal heterogeneity, with UiO-66 crystallites distinguishable from the a_gZIF-UC-7 (Fig. S26, ESI†) by atomic and wt% ratios. EDX mapping also confirms distinct microdomains (Fig. S27–S30, ESI†).

Pair distribution function (PDF) analysis confirms the structural integrity of the phases.[19] The structure factor, $S(Q)$,[20] of UiO-66 show Bragg peaks (Fig. S31a, ESI†) consistent with its crystal structure; Bragg peaks are not present in the $S(Q)$ of a_gZIF-UC-7 because of its amorphous glass structure (Fig. S31b, ESI†). The [(UiO-66)$_{0.5}$(a_gZIF-UC-7)$_{0.5}$] composite retained the UiO-66 Bragg features, indicating its preservation during composite synthesis (Fig. S32a, ESI†). $S(Q)$s of the composite and its physical mixture are largely similar, suggesting no decomposition or recrystallisation of the starting materials after composite fabrication (Fig. S32a, ESI†). Fourier transforming the $S(Q)$s produced the real-space $D(r)$ functions (PDFs).[22] The $D(r)$ from the pristine materials matched reported $D(r)$s (Fig. S33 and S34, ESI†),[7,21] and the composite and physical mixture $D(r)$s were nearly identical (Fig. S32b, ESI†), with short-range correlations from both starting materials (Fig. 2b) and longer-range peaks (beyond ∼8 Å) arising from UiO-66 (See ESI† for assignment of starting materials' $D(r)$s). The PDF results show that both phases were maintained after composite formation. Thermal stability was evaluated by TGA (Fig. S35–S37, ESI†), which shows T_ds of 411 °C and 425 °C for the physical mixture and composite respectively. DSC analysis on the physical mixture and composite show a peak at ∼100 °C in the first DSC upscan, corresponding to water evaporation, also present in the TGA of of UiO-66 (Fig. S38, ESI†). The a_gZIF-UC-7 T_g (∼273 °C) is present in both DSC upscans of the physical mixture and [(UiO-66)$_{0.5}$(a_gZIF-UC-7)$_{0.5}$], indicating structural preservation of the a_gZIF-UC-7.

The CO_2 uptake of ZIF-UC-7 (51.1 cm^3 g^{-1}), a_gZIF-UC-7 (14.8 cm^3 g^{-1}) and UiO-66 (95.0 cm^3 g^{-1}) matched reported literature values.[7] The [(UiO-66)$_{0.5}$(a_gZIF-UC-7)$_{0.5}$] composite, however, exhibits a CO_2 uptake of 30.9 cm^3 g^{-1} (Fig. 3a and Table S8, ESI†), indicating enhanced gas sorption capacity because of UiO-66 incorporation into the glass matrix. For N_2 adsorption, the a_gZIF-UC-7 glass has slightly higher uptake and BET surface area (55.4 m^2 g^{-1}) than its crystalline parent ZIF-UC-7 (41.8 m^2 g^{-1}), similar to previous analysis on crystalline ZIF-62 and its glass (Table S9, ESI†).[22] The composite and UiO-66 have BET surface areas of 214 and 852 m^2 g^{-1} respectively (Fig. 3b), confirming increased surface area when the UiO-66 is added to the glass matrix. Pore widths for ZIF-UC-7 and its glass could not be determined by N_2 and CO_2 adsorption because of gas size limitations, but the composite exhibits pore widths similar to the UiO-66 (Fig. S33, ESI†).

To evaluate biomedical potential, the pH stability of [(UiO-66)$_{0.5}$(a_gZIF-UC-7)$_{0.5}$], a_gZIF-UC-7 and UiO-66 in phosphate-buffered saline (PBS) solution was monitored over time (Fig. 3c). PBS, with a physiological pH of 7.4, mimics the

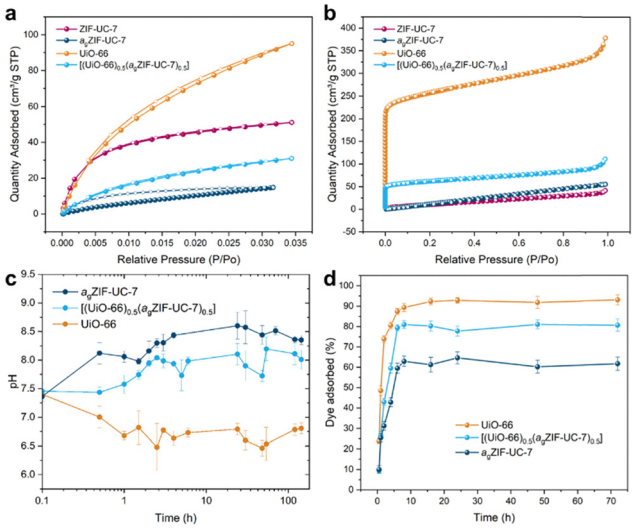

Fig. 3 a) CO_2 gas sorption isotherms for all the materials at 273 K. (b) N_2 gas sorption isotherms for all the materials at 77 K. Open and closed circles represent adsorption and desorption respectively. (c) pH stability tests in PBS over a 4 day period. (d) Methylene blue uptake over time, concentration of the starting solution was 5 ppm. UV-vis maximum was fixed at 664 nm (see Experimental methods).

concentration of ions in the human body and is widely used in biomedical research.[23] The pH increased over time for a_gZIF-UC-7, likely due to imidazolate linker release, previously shown by ZIF-8, [Zn(mIm)$_2$], where mIm is 2-methylimidazolate. UiO-66 immersion caused a decrease in pH, attributed to phosphate-induced degradation and terephthalate release.[24,25] In contrast, [(UiO-66)$_{0.5}$(a_gZIF-UC-7)$_{0.5}$] showed minimal pH changes, maintaining a stable environment, which is crucial for biomedical applications because it can protect drugs from environment-induced degradation and allow for slower release of encapsulated drugs within the composite.[26] Moreover, after PBS immersion, the composite maintains its N_2 uptake, suggesting its suitability for drug capture in PBS media (Table S8 and Fig. S39, S40, ESI†). Optical and SEM images after 24 hours in PBS show that the composite retains its surface morphology, with UiO-66 crystallites visible in the composite (Fig. S41 and S42, ESI†). EDX analysis gives a Zr : Zn ratio of 1.3–1.9 (Fig. S43 and S44, ESI†), suggesting minimal degradation of either component and microdomains are still visible in the EDX mapping (Fig. S45, ESI†). ICP-OES analysis shows a small decrease in the Zr : Zn ratio (1 : 1.23 to 1 : 1.07) after PBS immersion, likely from a_gZIF-UC-7 leaching into the PBS solution (Table S10, ESI†).[23] This is corroborated by the higher Zr : Zn ratio of 1 : 1.74 in the PBS supernatant. PXRD analysis on the UiO-66 control after immersion in PBS containing 5 ppm of methylene blue (MB) over 24 hours confirms UiO-66's degradation, given by a lack of Bragg peaks (Fig. S46, ESI†). However, in the composite, UiO-66 retained its crystallinity, highlighting the a_gZIF-UC-7 matrix's ability to effectively stabilise the UiO-66 structure in PBS and prevent its degradation.

To assess drug delivery ability of the composite, MB dye was used as a proxy; UiO-66 efficiently adsorbs MB in neutral/basic

Open Access Article. Published on 16 July 2025. Downloaded on 5/23/2026 10:59:14 AM.
This article is licensed under a Creative Commons Attribution-NonCommercial 3.0 Unported Licence.

solutions.[27] Samples were immersed in 5 ppm MB solutions in PBS (Fig. 3d), reaching 92%, 62%, and 81% adsorption for UiO-66, a_gZIF-UC-7 and the composite respectively after 8 hours. Despite a lower UiO-66 molar ratio, the composite's adsorption is similar to the pristine UiO-66, likely because of its stable pH (the adsorption capacity of UiO-66 increases as pH increases).[27] PXRD (Fig. S46, ESI†) shows that UiO-66 degrades after 24 hours, while the composite retains Bragg peaks, highlighting UiO-66's improved stability in the glass matrix.

In conclusion, this study reports the synthesis of a novel MOF CGC by dispersing UiO-66 in a_gZIF-UC-7. FTIR, PDF, and PXRD confirmed the preservation of the starting materials, while DSC scans showed the expected T_g of a_gZIF-UC-7. The $[(\text{UiO-66})_{0.5}(a_g\text{ZIF-UC-7})_{0.5}]$ composite combines UiO-66's high surface area, gas sorption, and dye uptake with the amorphous flexibility of a_gZIF-UC-7. Enhanced CO_2 uptake and BET surface area reflect the benefits of embedding UiO-66 in the glass matrix. The composite's superior pH stability in PBS, compared to UiO-66, highlights the matrix's protective role. Efficient methylene blue adsorption of the composite, despite its lower UiO-66 content, confirms MOF preservation post immersion. These findings suggest promising applications in gas storage, biomedical devices, drug delivery and environmental remediation, paving the way for future MOF CGC research.

AMC and CCB acknowledge Leverhulme Trust Research (RPG-2020-005). CCB also thanks Comunidad de Madrid (2024-T1/TEC-31450). TDB thanks the Royal Society (URF\R\211013, RGS\R2\212221). We acknowledge to Diamond Light Source (I15-1, CY29957). LNM and BT (Faculty of Science and Engineering) thank the University of Liverpool for funding.

CCB conceptualised the project. AMC, YR and CCB wrote the manuscript with input from all authors. YR and CCB synthesised all materials. YR conducted FTIR, SEM-EDX, PXRD, TGA and DSC analysis under CCB and AMC's supervision. CCB, GPR, PAC, DAK, and AK collected PDF data, processed by AMC. TDB funded the work and contributed with discussions. BT and LNM collected gas sorption data, analysed by CCB. CCB conducted dye uptake experiments and analysis.

Conflicts of interest

There are no conflicts to declare.

Data availability

The data supporting this article have been included as part of the ESI† for SEM, ICP and pH stability tests. Data for this article, including DSC, PXRD, PDF, FTIR, TGA, gas sorption isotherms and UV-vis are available at Open Science Framework at DOI **https://doi.org/10.17605/OSF.IO/QY8ZT**.

References

1 H. Furukawa, K. E. Cordova, M. O'Keeffe and O. M. Yaghi, *Science*, 2013, **341**, 1230444.
2 A. Dhakshinamoorthy, Z. Li and H. Garcia, *Chem. Soc. Rev.*, 2018, **47**, 8134–8172.
3 J. Yang and Y.-W. Yang, *Small*, 2020, **16**, 1906846.
4 T. D. Bennett, Y. Yue, P. Li, A. Qiao, H. Tao, N. G. Greaves, T. Richards, G. I. Lampronti, S. A. T. Redfern, F. Blanc, O. K. Farha, J. T. Hupp, A. K. Cheetham and D. A. Keen, *J. Am. Chem. Soc.*, 2016, **138**, 3484–3492.
5 L. Frentzel-Beyme, M. Kloß, P. Kolodzeiski, R. Pallach and S. Henke, *J. Am. Chem. Soc.*, 2019, **141**, 12362–12371.
6 L. León-Alcaide, R. S. Christensen, D. A. Keen, J. L. Jordá, I. Brotons-Alcázar, A. Forment-Aliaga and G. Mínguez Espallargas, *J. Am. Chem. Soc.*, 2023, **145**, 11258–11264.
7 A. M. Bumstead, C. Castillo-Blas, I. Pakamorė, M. F. Thorne, A. F. Sapnik, A. M. Chester, G. Robertson, D. J. M. Irving, P. A. Chater, D. A. Keen, R. S. Forgan and T. D. Bennett, *Chem. Commun.*, 2023, **59**, 732–735.
8 J. Kahr, J. P. S. Mowat, A. M. Z. Slawin, R. E. Morris, D. Fairen-Jimenez and P. A. Wright, *Chem. Commun.*, 2012, **48**, 6690–6692.
9 L. Longley, N. Li, F. Wei and T. D. Bennett, *R. Soc. Open Sci.*, 2017, **4**, 171355.
10 I. Abánades Lázaro and R. S. Forgan, *Coord. Chem. Rev.*, 2019, **380**, 230–259.
11 J. Ren, H. W. Langmi, B. C. North and M. Mathe, *Int. J. Energy Res.*, 2015, **39**, 607–620.
12 N. Yuan, X. Zhang and L. Wang, *Coord. Chem. Rev.*, 2020, **421**, 213442.
13 S. Yang, L. Peng, S. Bulut and W. L. Queen, *Chem. – Eur. J.*, 2019, **25**, 2161–2178.
14 Y. Cheng, S. J. Datta, S. Zhou, J. Jia, O. Shekhah and M. Eddaoudi, *Chem. Soc. Rev.*, 2022, **51**, 8300–8350.
15 Y. Zhang, X. Feng, S. Yuan, J. Zhou and B. Wang, *Inorg. Chem. Front.*, 2016, **3**, 896–909.
16 T. D. Bennett, Y. Yue, P. Li, A. Qiao, H. Tao, N. G. Greaves, T. Richards, G. I. Lampronti, S. A. T. Redfern, F. Blanc, O. K. Farha, J. T. Hupp, A. K. Cheetham and D. A. Keen, *J. Am. Chem. Soc.*, 2016, **138**, 3484–3492.
17 C. W. Ashling, D. N. Johnstone, R. N. Widmer, J. Hou, S. M. Collins, A. F. Sapnik, A. M. Bumstead, P. A. Midgley, P. A. Chater, D. A. Keen and T. D. Bennett, *J. Am. Chem. Soc.*, 2019, **141**, 15641–15648.
18 D. Zou and D. Liu, *Mater. Today Chem.*, 2019, **12**, 139–165.
19 C. Castillo-Blas, J. M. Moreno, I. Romero-Muñiz and A. E. Platero-Prats, *Nanoscale*, 2020, **12**, 15577–15587.
20 D. A. Keen, *J. Appl. Crystallogr.*, 2001, **34**, 172–177.
21 J. Hou, C. W. Ashling, S. M. Collins, A. Krajnc, C. Zhou, L. Longley, D. N. Johnstone, P. A. Chater, S. Li, M. V. Coulet, P. L. Llewellyn, F. X. Coudert, D. A. Keen, P. A. Midgley, G. Mali, V. Chen and T. D. Bennett, *Nat. Commun.*, 2019, **10**, 2580.
22 L. Frentzel-Beyme, P. Kolodzeiski, J.-B. Weiß, A. Schneemann and S. Henke, *Nat. Commun.*, 2022, **13**, 7750.
23 M. D. J. Velásquez-Hernández, R. Ricco, F. Carraro, F. T. Limpoco, M. Linares-Moreau, E. Leitner, H. Wiltsche, J. Rattenberger, H. Schröttner, P. Frühwirt, E. M. Stadler, G. Gescheidt, H. Amenitsch, C. J. Doonan and P. Falcaro, *CrystEngComm*, 2019, **21**, 4538–4544.
24 I. Abánades Lázaro, S. Haddad, S. Sacca, C. Orellana-Tavra, D. Fairen-Jimenez and R. S. Forgan, *Chem*, 2017, **2**, 561–578.
25 D. Bůžek, S. Adamec, K. Lang and J. Demel, *Inorg. Chem. Front.*, 2021, **8**, 720–734.
26 H. Kaur, G. C. Mohanta, V. Gupta, D. Kukkar and S. Tyagi, *J. Drug Delivery Sci. Technol.*, 2017, **41**, 106–112.
27 A. A. Mohammadi, A. Alinejad, B. Kamarehie, S. Javan, A. Ghaderpoury, M. Ahmadpour and M. Ghaderpoori, *Int. J. Environ. Sci. Technol.*, 2017, **14**, 1959–1968.